Extended Abstracts of the 2009 International Conference on Solid State Devices and Materials, Sendai, 2009, pp50-51

Lanthanoid Metal Oxide MIM Capacitors for Precision Analog Circuits: Material Screening, Process Development, and Characterization

Jing-De Chen[1], Jian-Jun Yang[1], Rick Wise[2], Philipp Steinmann[2], Chunxiang Zhu[1], and Yee-Chia Yeo[1,*]

[1]Dept. of Electrical & Computer Eng., National University of Singapore, Singapore 117576. [2] Texas Instruments Inc., Dallas, TX, USA.

[*] Tel: +65 6516 2298; Fax: +65 67791103; Email: yeo@ieee.org

I. Introduction

Metal-insulator-metal (MIM) capacitors occupy substantial areas in integrated circuits for radio-frequency (RF) and analog/mixed-signal applications. Increasing the capacitance density enables smaller die sizes. A high capacitance density should be achieved without compromising the voltage coefficient of capacitance (VCC) and leakage current. High-κ dielectrics have been investigated to replace the conventional SiO_2 and SiON in MIM capacitors [1]-[2]. High-κ (κ~20) lanthanoid metal oxides have attracted much attention [3]. However, a systematic study of lanthanoid metal oxides for the application in RF and analog/mixed-signal MIM capacitors has not been performed except for La_2O_3 [4]. In this paper, we report the first investigation of a series of oxides of lanthanoid elements (La, Gd, Tb, Dy, Er, and Yb) for MIM capacitor applications. Er_2O_3 was found to be very promising. We further discuss the optimization and electrical characterization of MIM capacitors with Er_2O_3 dielectric.

II. Experiments

MIM capacitors were fabricated on Si wafers covered with 400 nm thick SiO_2. A 200 nm thick TaN bottom electrode layer was sputter-deposited. Lanthanoid dielectrics (La_2O_3, Gd_2O_3, Dy_2O_3, Er_2O_3, and Yb_2O_3) were reactively sputtered from metal targets in Ar/O_2 ambient with various Ar/O_2 ratios, while the total gas flow was fixed at 30 sccm. Post deposition annealing (PDA) was performed in 3 different ambient: (1) 100% N_2 with no O_2, (2) trace O_2, or (3) 95% N_2 mixed with 5% O_2. For the process with "trace O_2", the N_2 gas flow contained 5% O_2 before temperature ramp-up, but there was no O_2 flow afterwards. Finally, a 150 nm thick TaN top electrode layer was formed by sputtering and patterning using dry etching. The MIM device structure and process flow are shown in Fig. 1.

III. Results and discussions

(a) Material Screening

Table I lists the lanthanoid oxides investigated. All these oxides have energy gaps close to or larger than 5 eV, except Tb_2O_3. Fig. 2 compares the quadratic VCC α of MIM capacitors with 6 different dielectrics. Data presented in Fig. 2 are the best ones for each oxide obtained from a first round of process optimization (Section II). The black line represents the highest capacitance density for a given α and is contributed by data points from Er_2O_3. MIM capacitors with Er_2O_3 dielectric have lowest α (positive) for a given capacitance density. Fig. 3 compares the leakage current density *J* at +3.3 V for all 6 materials. Er_2O_3 dielectric gives the lowest leakage current (black line) for a given capacitance density. Er_2O_3 outperforms all other 5 candidates in both quadratic VCC and leakage current; it is also better than other high-κ materials reported in literature, which will be discussed later.

(b) Process Development of Er_2O_3 MIM capacitors

To optimize the performance of Er_2O_3 MIM capacitors, we varied the ambient oxygen concentration during deposition and PDA. Fig. 4 shows the capacitance obtained at the different process conditions. For the 12 nm split, the capacitance density drops significantly with increased O_2 in PDA process; this is due to the oxidation of bottom TaN electrode. However, there is no significant capacitance change for 24 nm and 36 nm splits. Fig. 5 demonstrates typical *C-V* curves of MIM capacitors with 12 nm Er_2O_3, where the quadratic α and linear VCC β are extracted. Fig. 6 summarizes α values for all thicknesses and process conditions. Thinner oxides show larger α. For each thickness, capacitors annealed in trace O_2 ambient demonstrate smaller α than the other two PDA conditions with less or more oxygen. This implies that a proper amount of O_2 is helpful in maintaining a small α. The capacitor with Er_2O_3 sputtered using 2 sccm O_2 exhibits significantly higher α comparing to one with Er_2O_3 sputtered in 3 sccm O_2, although their thicknesses and capacitance densities are almost the same. This indicates that the oxygen vacancies induced in the sputtering process has a large impact on α. Linear VCC β values are summarized in Fig. 7. β is related to asymmetric device structure. β reduces with increased oxygen concentration during PDA, and the effect is less pronounced for thicker oxides; this can be explained by a more uniform dielectric layer with less oxygen vacancies. The leakage current *J* of 24 nm Er_2O_3 is shown in Fig. 8. *J* is at the order of 10^{-8} at ±3.3 V bias; the split with trace O_2 during PDA has a smaller *J* than the other two. Considering the results discussed above, we decided the optimized process condition for Er_2O_3 deposition to be: 3 sccm O_2 flow in sputter and trace O_2 in PDA process. The following characterization was all performed on devices formed with this process condition.

(c) Electrical Characterization of Er_2O_3 MIM capacitors

Fig. 9 shows the capacitance densities and loss tangent of MIM capacitors with Er_2O_3 dielectric as a function of frequency. The loss of capacitance from 1 kHz to 200 kHz are 0.68%, 0.8% and 1.1%, for 12 nm, 24 nm, and 36 nm Er_2O_3 MIM capacitors, respectively. The loss tangent increases from ~10^{-4} at 1 kHz to ~10^{-2} at 200 kHz for all samples. The frequency dispersion of α and β are shown in Fig. 9 and Fig. 10, respectively. Log(α) decreases linearly with a logarithmic increase in frequency. The frequency dependence of α can be explained as the change of relaxation time with different carrier mobility in insulator [6]. β decreases with increasing frequency for 24 nm and 36 nm Er_2O_3 capacitors, but increases for the 12 nm split. This is due to different electrode/dielectric interface conditions. Fig. 11 shows the temperature dependence of capacitance (TCC). 24 nm and 36 nm samples both show acceptable TCC of ~180 ppm/°C. The smaller TCC for 12 nm sample might be due to the interfacial layer caused by the oxidation of bottom electrode. Literature data on high-κ MIM capacitors are summarized and compared in Table II. In comparison with the data in literature, MIM capacitors with PVD Er_2O_3 dielectric show high capacitance density, low leakage current, low α, acceptable β and small TCC, suggesting its potential use in future RF and analog/mixed signal IC applications.

IV. Conclusion

We systematically studied 6 lanthanoid oxides as dielectrics in MIM capacitors for RF and analog/mixed-signal circuits. Among those oxides, Er_2O_3 outperforms others in quadratic VCC and leakage current. With process optimization, Er_2O_3 MIM capacitors achieve high capacitance densities ranging from 5.8 to 18.4 $fF/\mu m^2$, low VCC and TCC values, and low leakage current at around 1×10^{-8} A/cm^2.

Acknowledgement. This work was supported by Texas Instruments through a Semiconductor Research Corporation (SRC) grant and also by National Research Foundation (Award number NRF-RF2008-09).

References

[1] H. Hu *et al.*, *IEEE EDL* 23, pp. 514, 2002.
[2] Y. L. Tu *et al.*, *Symp. VLSI Tech. Dig. 2003*, pp. 79.
[3] S. Jeon *et al.*, *IEDM Tech. Dig. 2001*, pp. 471.
[4] M. Y. Yang *et al.*, *J. Electrochem. Soc.* 151, pp. 162, 2004
[5] A. V. Prokofiev *et al.*, *J. All. Comp*. 242, 41, 1996.
[6] C. Zhu *et al.*, *IEDM Tech. Dig. 2003*, pp. 879.
[7] J. H. Lee *et al.*, *IEEE Microwave Lett.* 9, pp. 345, 1999.
[8] M. Armacost *et al.*, *IEDM Tech. Dig. 2000*, pp. 157.
[9] P. Zucher *et al.*, *IEDM Tech. Dig. 2000*, pp. 153.
[10] S. Huylenbroeck *et al.*, *IEEE EDL* 23, pp. 191, 2002.
[11] C. H. Ng *et al.*, *IEDM Tech. Dig.* 2002, pp. 241.
[12] Y. K. Jeong *et al.*, *Symp. VLSI Tech. Dig. 2004*, pp. 222.
[13] S. B. Chen *et al.*, *IEEE EDL* 23, pp. 185, 2002.
[14] X. F. Yu *et al.*, *IEEE EDL* 24, pp. 63, 2003.
[15] S. J. Kim *et al.*, *Symp. VLSI Tech. Dig. 2003*, pp. 77.

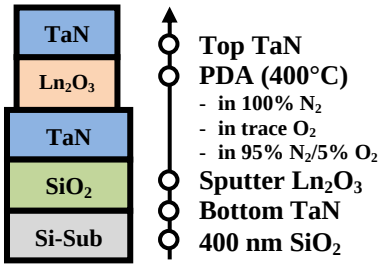

Fig. 1. MIM capacitor structure and process flow.

Table I: Comparison of physical properties of selected lanthanoid elements and their sesquioxides [5].

	La	Gd	Tb	Dy	Er	Yb
Atomic Number	57	64	65	66	68	70
Oxide	La_2O_3	Gd_2O_3	Tb_2O_3	Dy_2O_3	Er_2O_3	Yb_2O_3
Band-gap (eV)	5.6	5.4	3.8	4.9	5.3	4.9

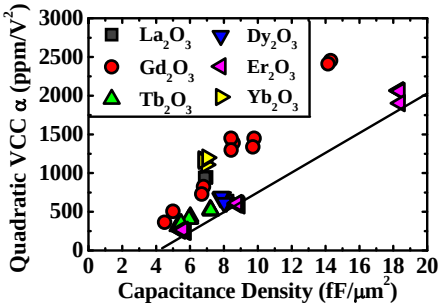

Fig. 2. Quadratic VCC versus capacitance density for all lanthanoid oxide MIM capacitors.

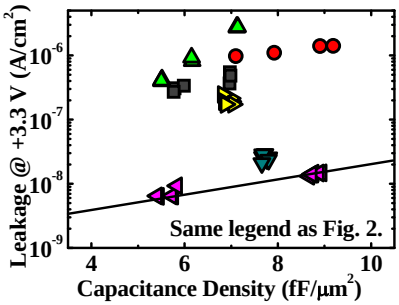

Fig. 3. Leakage current at +3.3V plotted versus capacitance density for all lanthanoid oxide MIM capacitors.

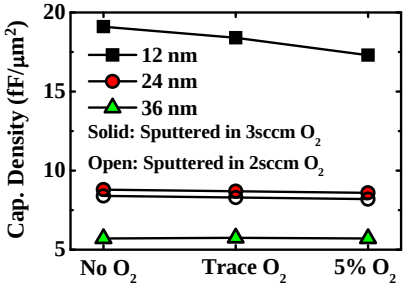

Fig. 4. Capacitance densities against different oxygen concentrations in PDA ambient.

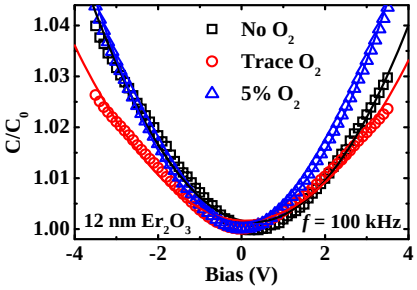

Fig. 5. Normalized *C-V* curves of 12 nm Er_2O_3 MIM capacitors. The solid lines are polynomial fitted curves.

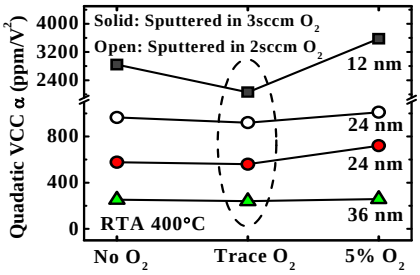

Fig. 6. Quadratic VCC α against different oxygen concentrations in PDA ambient.

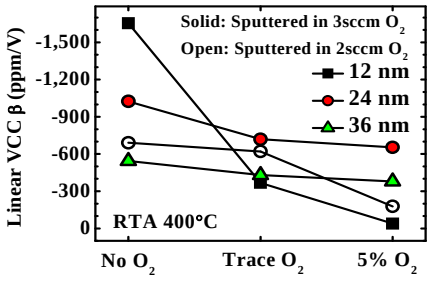

Fig. 7. Linear VCC β against different oxygen concentrations in PDA ambient.

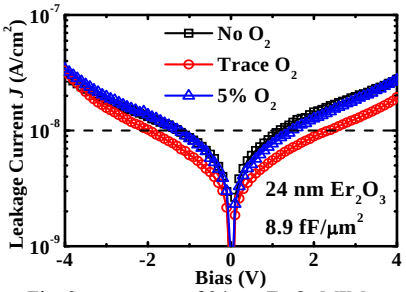

Fig. 8. *J-V* curves of 24 nm Er_2O_3 MIM capacitors with different oxygen concentrations in PDA ambient.

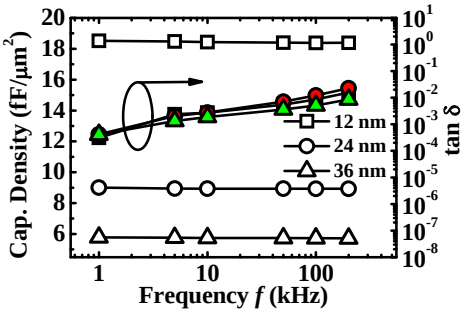

Fig. 9. Frequency dispersion of capacitance density and loss tangent.

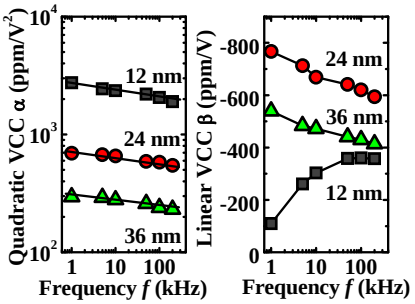

Fig. 10. Frequency dispersion of quadratic VCC α and linear VCC β.

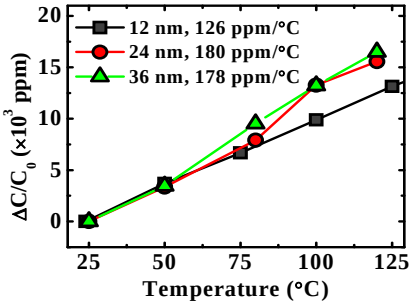

Fig. 11. Temperature dependence of capacitance density. TCC values are small.

Table II. Comparison of DC performance of reported binary high-K MIM capacitors

	Dielectrics	Cap. Density (fF/μm²)	J_{leak} @ 1 V (A/cm²)	J_{leak} @ 3.3 V (A/cm²)	α @ 100kHz (ppm/V²)	β @ 100kHz (ppm/V)	TCC
SiO_2/Si_3N_4 MIM	SiO_2, ONO, Si_3N_4 [7-11]	1~2	1E-7~1E-9	N/A	10~70	10~160	40~130
High-κ MIM	Ta_2O_5 [12]	4	N/A	6E-5	-9.9	N/A	106
	Al_2O_3 [13]	5.2	4.3E-8	N/A	2051	1888	109~208
	ALD HfO_2 [14]	8	~4E-8	~6E-7	~1800	~4000	N/A
	La_2O_3 [4]	9.2	<1E-5	N/A	~3000	~3000	347
	PVD HfO_2 [15]	13.7	N/A	4E-4@125°C	4631	-4843	135
Our results	Er_2O_3 (36 nm)	5.8	3.5E-9	~6.4E-9	240	-430	178
	Er_2O_3 (24 nm)	8.9	5.5E-9	~1.4E-8	580	-620	170
	Er_2O_3 (12 nm)	18.4	1.3E-8	~4.9E-7	2000	-360	126